JOURNAL OF ELECTROMAGNETIC ENGINEERING AND SCIENCE, VOL. 23, NO. 5, 429~436, SEP. 2023

https://doi.org/10.26866/jees.2023.5.r.188
ISSN 2671-7263 (Online) · ISSN 2671-7255 (Print)

An I-Shaped Slot Grid Antenna Array with Substrate Integration and Enhanced Bandwidth

Zhiyi Li · Shengjie Wang · Fan Li · Lin Lin · Hongzheng Zeng*

Abstract

Aimed to transmit electromagnetic energy in wireless power transfer, a planar substrate-integrated grid antenna array with four I-shaped slots was designed. A transverse stub was added to the microstrip line to produce additional resonance; hence, the impedance bandwidth was enhanced from 1.9% to 6%. Four I-shaped slots were formed on a perfect electric conductor (PEC) sheet to realize boresight radiation. Four gaps were etched to refine and compress the in-band impedance property. Furthermore, characteristic mode theory was adopted to analyze the working mechanism. Finally, the measurement results showed that the antenna had an operating bandwidth of 5% ($|S_{11}| < -10$ dB from 5.67 GHz to 5.96 GHz). In the operating band, the boresight gain varied from 9.3 dBi to 11.3 dBi. The cross-polarization level was lower than −30 dB on the boresight. Therefore, the proposed array is suitable for use in wireless power transfer systems and other related applications.

Key Words: CMA, Grid Antenna Array, I-Shaped Slot, Substrate Integration, Wireless Power Transfer.

I. Introduction

Unlike traditional wire transport technology, wireless power transfer (WPT) is a novel approach to transmitting energy through free space [1–4]. To adapt to diversified WPT scenarios, different types of transmitting antennas have been proposed, such as wearable [5], implantable [6], electrically small [7], and reconfigurable [8]. To improve the transfer efficiency of a WPT system in the 5.8 GHz ISM band, antennas with high gain and planar structures are urgently required [9]. A high-gain antenna can reduce transmitting power and hence simplify a transmitter configuration. A planar antenna can be easily integrated into a TX/RX end and make a system more compact.

Nowadays, many transmitting antennas with high gain and planar structures have been used in WPT systems [10–14]. By adopting a superstrate, a high-gain array antenna working in its high-order mode has been proposed [10]. Due to the reflection of the metal ground and the concentration of the superstrate, the boresight gain was up to 24.2 dBi. Similarly, the Luneburg lens is employed as an artificial dielectric superstrate to improve the peak gain of the horn-like antenna [11]. The peak gain was up to 17.2 dBi. To implement a WPT experiment in any three-dimensional space, a transmitting antenna array with 8 × 8 elements was designed [12].

In 2019, a double-sided S-shaped gradient-refractive index metamaterial (GRIN MM) unit cell was designed to enhance radiation in the far field; hence, the gain was promoted [13]. In 2022, a dual-polarized hybrid antenna was proposed for both radio frequency-energy harvesting (RF-EH) and WPT applications [14]. In that work, a 2 × 2 patch array was designed, and the gain was up to 11.8 dBi.

Manuscript received December 14, 2022 ; Revised February 8, 2023 ; Accepted June 7, 2023. (ID No. 20221214-177J)
CAAC Key Laboratory of Flight Techniques and Flight Safety, Civil Aviation Flight University of China, Guanghan, China.
*Corresponding Author: Hongzheng Zeng (e-mail: Zeng.H.Z@outlook.com)

In the last few years, substrate-printed antennas and grid antennas have attracted many designers due to the advantages of low price, small size, suitability for mass production, and ease of integration [15–24]. By forming an array with substrate-printed elements, both high gain and high integration can be obtained simultaneously. Additionally, the characteristic mode (CM) theory has developed rapidly in recent years [25–29]. Characteristic mode analysis (CMA), based on CM theory, provides novel insights into the working mechanism of an antenna structure. Hence, analyzing and guiding antenna design by adopting CM theory has become a priority for antenna developers.

In this current study, the objective was to design an I-shaped slot grid antenna array with planar substrate integration and enhanced bandwidth for a 5.8 GHz WPT application. The main innovations are listed below. First, a transverse stub was introduced to produce a new resonant point; hence, the bandwidth was enhanced. Second, four gaps were etched to refine the in-band impedance matching. Third, CMA was implemented to analyze the surface current distribution of the grid antenna. Also, two pieces of substrates were integrated to make the antenna compact, and an I-shaped slot was adopted as the basic radiation element to obtain more design freedom when compared with a rectangular slot. A microstrip line was introduced to make the front-end feeding circuit easily printed on the back of the antenna. Finally, the operating band of the proposed array could cover the 5.8 GHz ISM band (5.725–5.875 GHz). The measured peak gain was up to 11.3 dBi. Simulation and measurement results agreed well with each other.

II. Antenna Geometry

The overall view of the proposed grid antenna array is presented in Fig. 1(a). The main structure was composed of two pieces of Taconic TLX substrates with relative permittivity ε_r = 2.55. By punching eighteen screw holes in different locations, the two substrates were spliced together by nylon screws. A perfect electric conductor (PEC) sheet was printed on the top face of the upper substrate. Four identical I-shaped slots were etched on the sheet; hence, a grid structure was formed, as shown in Fig. 1(c). An enlarged view of the I-shaped slot is shown in Fig. 1(b). Four gaps were etched on the edge of the PEC sheet to refine impedance matching. The bottom face of the upper substrate is shown in Fig. 1(d), on which no metallic layer is printed. Additionally, twenty-two metallic vias were punched in the upper substrate to connect the PEC sheet to the ground. The top face of the lower substrate is the ground layer, as shown in Fig. 1(e). An aperture was etched on the ground layer to couple the electromagnetic (EM) signal to the top PEC sheet. On the bottom face of this substrate, a microstrip line with 50 Ω characteristic impedance was printed to receive the signal from the front-end

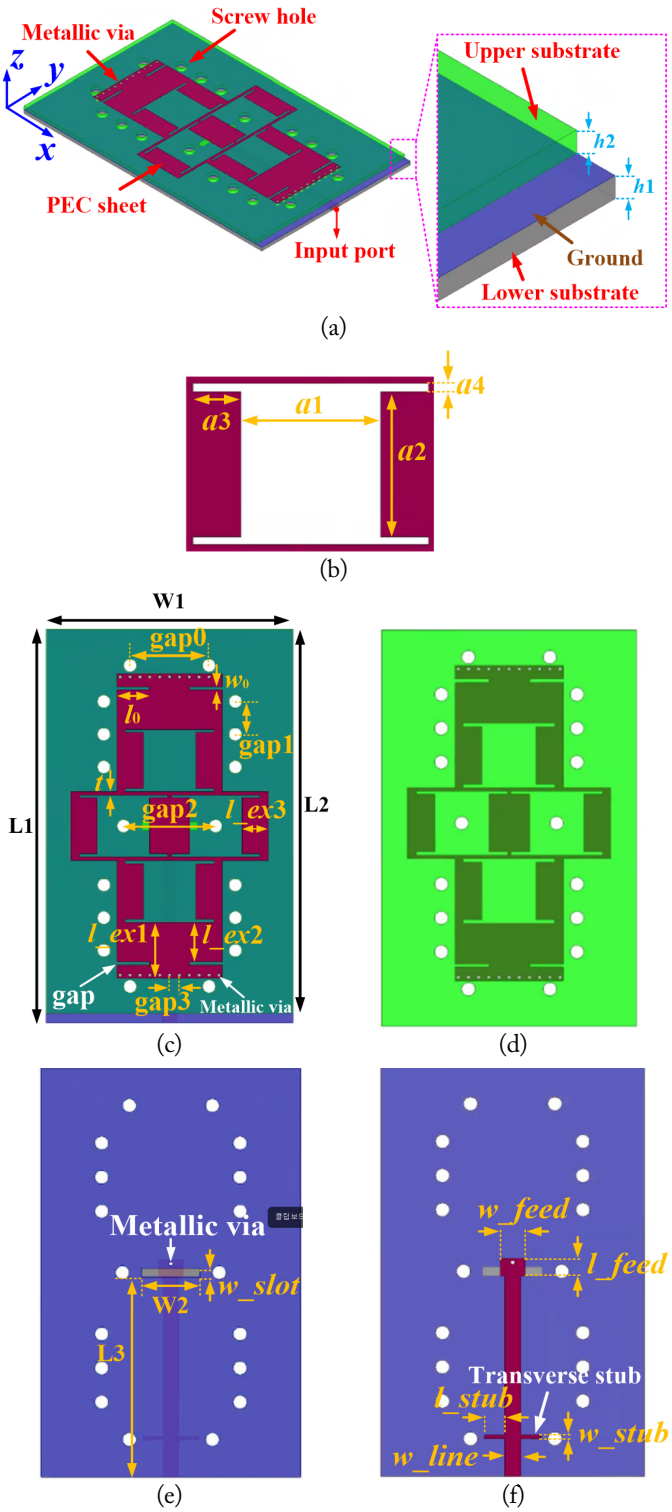

Fig. 1. View of the I-shaped slot grid antenna: (a) overall view, (b) I-shaped slot, (c) top and (d) bottom face of the upper substrate, (e) top and (f) bottom face of the lower substrate.

feeding circuit, as shown in Fig. 1(f). The overall electrical size is 1.45λ × 2.32λ × 0.06λ (λ is the wavelength in free space at 5.8 GHz).

To avoid an open state at the end of the microstrip line, a metallic via was punched on the lower substrate; hence, the microstrip line and ground were electrically connected. Furthermore,

a transverse stub was added to the microstrip line to obtain a wider impedance bandwidth. By simulation and optimization, the final dimensions of the antenna are listed in Table 1.

III. Simulation and Analysis

To show the EM characteristics, the proposed antenna was built and simulated in commercial simulation software, High-Frequency Structure Simulator (HFSS). In this section, bandwidth enhancement, CMA, and radiation mechanisms are discussed in sequence.

1. Bandwidth Enhancement

To demonstrate bandwidth enhancement and refinement, the antennas with/without the transverse stub and gaps were simulated and compared simultaneously.

For simplicity, the antenna without the stub and gaps is called the original antenna. $|S_{11}|$ of the original antenna is shown in Fig. 2(a) with an illustration of the PEC sheet and microstrip line. Only one resonance occurred at 5.8 GHz in the plot. The relative bandwidth for $|S_{11}| < -10$ dB is 1.9% (5.76–5.87 GHz). To improve the bandwidth, a transverse stub was added to the microstrip line. As shown in Fig. 2(b), the length (*l_stub*) of the stub has a significant influence on $|S_{11}|$. With the increase of *l_stub*, one more resonant frequency appears at 5.95 GHz, and the original resonant point moved to 5.7 GHz. Here, *l_stub* = 7.8 mm was adopted in the design, and the relative bandwidth was expanded to 6% (5.65–6 GHz) for $|S_{11}| < -10$ dB, as shown by the pink curve in Fig. 2(b).

Table 1. Optimized dimensions of the proposed I-shaped slot grid antenna (unit: mm)

Parameter	Value	Parameter	Value
*a*1	16	gap3	3
*a*2	17	*l_ex*1	17
*a*3	5.5	*l_ex*2	12
*a*4	1	*l_ex*3	8
L1	120	*t*	1
L2	117	*w_slot*	2.5
L3	58.75	*l_feed*	5
W1	75	*w_feed*	7
W2	17	*l_stub*	5.8
l_0	10	*w_stub*	1
w_0	1	*w_line*	4.4
gap0	24	h_1	1.575
gap1	10	h_2	1.575
gap2	28	-	-

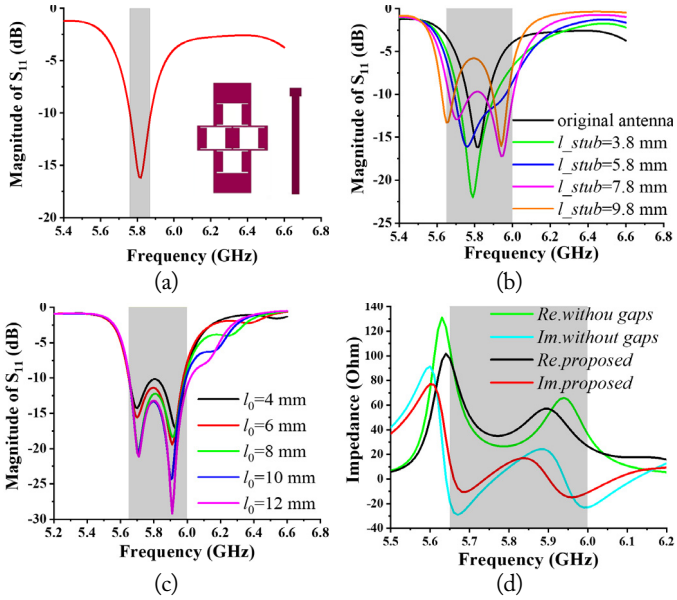

Fig. 2. (a) $|S_{11}|$ for original antenna, (b) $|S_{11}|$ for different *l_stub*, (c) $|S_{11}|$ for different l_0, and (d) impedance with/without gaps.

Also, four gaps (as shown in Fig. 1(c)) were etched on the PEC sheet to refine the impedance from 5.65 GHz to 6 GHz. As shown in Fig. 2(c), the influence of these gaps on $|S_{11}|$ was plotted. $|S_{11}|$ in-band (5.65–6 GHz) becomes smaller when l0 increases from 4 mm to 10 mm. While, $|S_{11}|$ almost keeps the same when l0 further increases to 12 mm. So, l_0 =10 mm is adopted in the design. To physically explain the refinement, the input impedance of the antennas with and without gaps is plotted in Fig. 2(d). In the concerning band (brown region), the black and red curves are more converged and closer to 50 Ω and 0 Ω when compared with the green and blue ones. In other words, these gaps compress the real and imaginary parts of the input impedance to 50 Ω and 0 Ω, respectively. Therefore, the bandwidth of the original antenna was enhanced and refined with the existence of a transverse stub and gaps. The final operating band ranges from 5.65 GHz to 6 GHz, which covers the transmitting frequency of 5.8 GHz in WPT.

2. CMA and Surface Current

Early CM theory is known to solve the electric field integral equations for a perfect electric conductor [25-29]. The equation involves a boundary condition of the perfect conductor, which can be presented by

$$[L(J)]_{tan} = E^i_{tan}(r) \tag{1}$$

where $L(\cdot)$ is an integro-differential operator to express the scattering field in terms of the current and can be written as follows:

$$[L(J)] = \frac{jk_0\eta_0}{4\pi}\left(\int_s J(r')G(r,r')dS' + \frac{1}{{k_0}^2}\nabla\int_s \nabla'\cdot J(r')G(r,r')dS'\right) \tag{2}$$

In Eq. (2), k_0 and η_0 are the wavenumber and wave impedance in free space. $G(r,r')$ is the Green's function multiplied by 4π in free space. By implementing a moment method to solve Eq. (1), the characteristic current on the surface of a scattering object can be obtained.

To explore the feasibility of the characteristic mode theory for the proposed antenna structure, CMA was adopted to analyze the surface current distribution and working mechanism at 5.8 GHz. According to the CM theory, the realistic total current (or radiation fields) can be decomposed into several characteristic currents (or characteristic fields) that are orthogonal to each other. In other words, characteristic modes (characteristic current or field) form a set of orthogonal basis vectors for any total current or total field distribution that may exist on an object. The decomposition can be mathematically explained by

$$J = \sum_n \alpha_n J_n, \tag{3}$$

where J and J_n are the realistic total current and characteristic current, respectively. α_n is the weighted coefficient of J_n.

As a key index in CMA, mode significance (MS) shows how easy it is for one mode to be motivated and is defined as

$$\mathrm{MS} = \frac{1}{|1+i\cdot\lambda_n|}, \tag{4}$$

where λ_n is the characteristic value of mode n, and MS is a real number between 0 and 1. For one mode, if its MS is near 1, this means that this mode is easy to excite. On the contrary, the mode is hard to be excited when its MS is close to 0.

As shown in Fig. 3, the MS of the first seven modes for the proposed grid antenna array is plotted. Three modes (mode 1, mode 5, and mode 7) with large MS (>0.707) are located at 5.04 GHz, 5.4 GHz, and 5.8 GHz, respectively. This means that the above three modes can easily be excited at these frequencies. Here, 5.8 GHz (black dash line) is located within the operating band of the proposed array. Thus, the working mechanism at 5.8 GHz can be explained through the characteristic current of mode 5. As shown in Fig. 4(a), the characteristic current at 5.8 GHz of mode 5 on the PEC sheet is plotted. The characteristic current on the upper edge of the I-shaped slot flows from side to center. The characteristic current on the lower edge flows from center to side. For comparison, the total current flow is

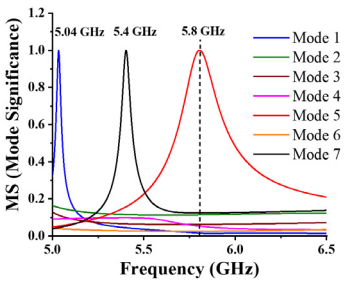

Fig. 3. The first seven MS of the proposed antenna array.

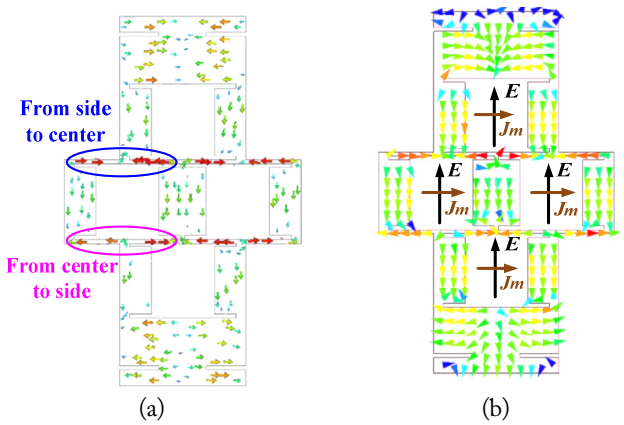

Fig. 4. (a) Characteristic current at 5.8 GHz of mode 5 and (b) total current distribution at 5.8 GHz.

plotted in Fig. 4(b). The characteristic current distribution of mode 5 is very similar to that of the total current distribution at 5.8 GHz. Therefore, it is concluded that the total current on the PEC sheet is dominated by mode 5. Other modes have little contribution to the total current at 5.8 GHz.

Also, the working mechanism of the I-shaped slot grid array can be seen equivalently as a magnetic dipole array with four elements. The general mathematical relationship between the equivalent magnetic current and the E-field in a slot can be expressed by

$$J_m = -n \times E, \tag{5}$$

where n is the normal direction of the slot. As shown in Fig. 4(b), the E-field in slots is marked by a black arrow, and the corresponding equivalent magnetic current is marked by a brown arrow.

Therefore, the working mechanism of the proposed I-shaped slot grid array is divided into two aspects at 5.8 GHz. On the one hand, the total surface current distribution on the PEC sheet was dominated by the characteristic current of mode 5. On the other hand, the radiation from the grid slots can be equivalent to the radiation of the magnetic dipole array, which will be discussed in the next section.

3. Radiation Mechanism Analysis

In this section, the radiating E-field at 5.8 GHz is discussed to explain the radiation mechanism. For simplicity, four I-shaped slots are named slot 1, slot 2, slot 3, and slot 4, respectively. The radiation field on the headroom of the antenna is shown in Fig. 5(a) and 5(b). From the top view in Fig. 5(a), four slots radiate their EM waves individually. The E-field from slots 2 and 3 is stronger than that from slots 1 and 4. From the side view in Fig. 5(b), the E-field from slot 1 and slot 4 is coupled to that of slot 2 and slot 3 after they depart from the surface of the antenna; hence, total boresight (z-axis in Fig. 1(a)) radiation is obtained. The boresight radiation was also validated by its 3D pattern,

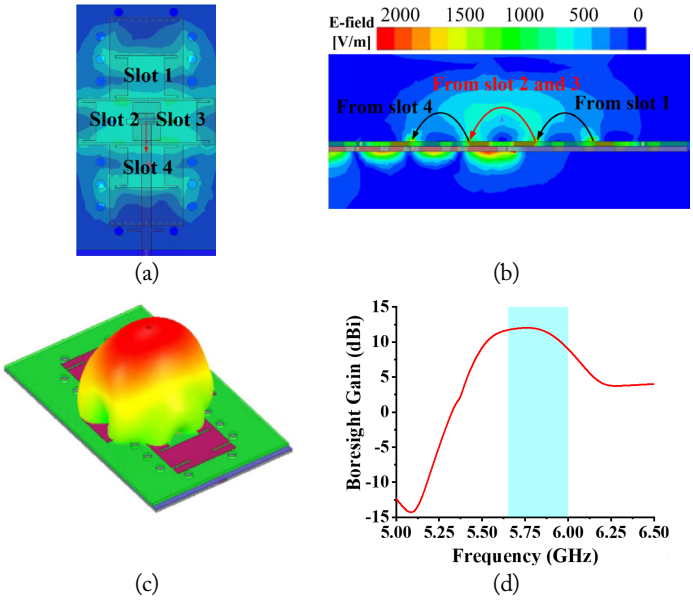

Fig. 5. Radiation E-field at 5.8 GHz: (a) top view, (b) front view, (c) 3D radiation pattern, and (d) boresight gain.

which is shown in Fig. 5(c). From the plot, maximum radiation occurs at the boresight of the antenna, and the gain is up to 12 dBi. The curve in Fig. 5(d) shows that the gain on boresight ranges from 9 dBi to 12 dBi in the blue zone. This guarantees stable boresight radiation across the entire operating band.

IV. Fabrication, Measurement, and Validation

To validate the design, a prototype was fabricated through a multi-layered substrate lamination technique. The PEC sheet was realized by copper plating. As shown in Fig. 6, the antenna was put into an anechoic chamber to measure its EM properties. The voltage standing wave ratio (VSWR) was obtained using the Agilent vector network analyzer N5230A.

As shown in Fig. 7, it is seen that the measured $|S_{11}|$ is less than -10 dB from 5.67 GHz to 5.96 GHz. Two resonant points are observed at 5.71 GHz and 5.89 GHz. Measured $|S_{11}|$ agreed well with the simulation. Fig. 8 gives both the simulated and measured normalized radiation patterns at 5.8 GHz. Due

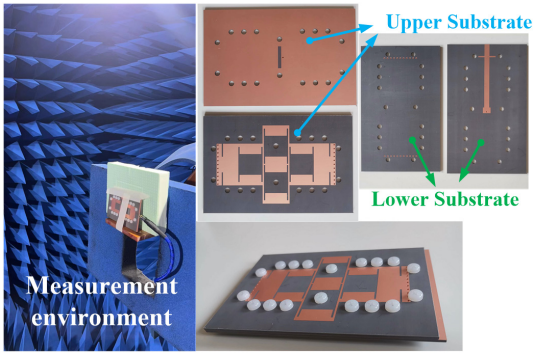

Fig. 6. Antenna prototype and measurement environment.

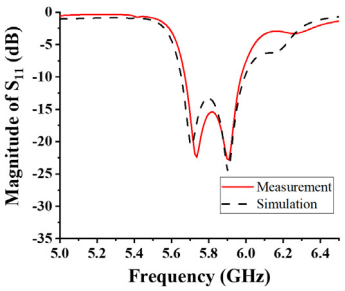

Fig. 7. Magnitude of S_{11} in simulation and measurement.

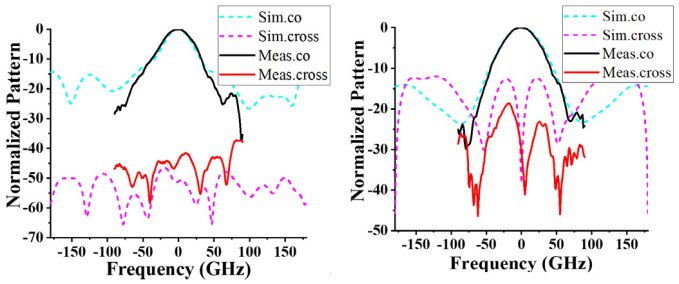

Fig. 8. Radiation patterns at 5.8 GHz for (a) the E-plane and (b) the H-plane.

to the limitation of our measurement environment, the measured angle is constrained between $-90°$ and $+90°$. From the patterns in both the E- and H-planes, the maximum radiation directs at the boresight of the antenna plane, and good agreement is observed between the simulation and the measurement. On the boresight, the measured cross-polarization level of measurement is less than -30 dB. A comparison between the simulated and measured gains on boresight is given in Fig. 9. In the operating band (yellow zone), the simulated and measured gains varied from 10 dBi to 12 dBi and from 9.3 dBi to 11.3 dBi, respectively. Peak gain (11.3 dBi) in measurement occurred at 5.76 GHz. The measured gain was 0.7 dB lower than that of the simulation, and the difference can be attributed to the substrate losses. According to the above discussion, the measurements and simulations agree well with each other, and the feasibility of the design is validated. The slight difference is caused by fabrication, installation, and measurement errors.

To show the performance advantage of the proposed antenna, Table 2 compares the proposed antenna and other related antennas. From the comparison, it is obvious that studies [11], [13], and

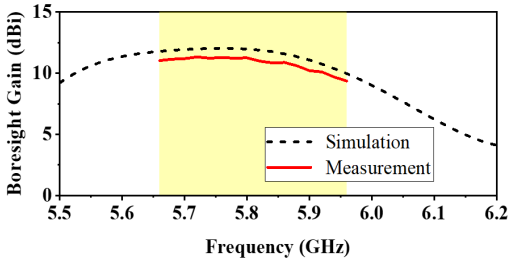

Fig. 9. Simulated and measured boresight gain.

Table 2. Performance comparison between the proposed antenna and other related published antennas in the WPT

Study	Bandwidth (%)	Gain (dBi)	Overall size
Chang et al. [5]	4.6	2.71 (2.4 GHz), 0.13 (5.2 GHz)	$0.65\lambda_0 \times 0.65\lambda_0$
Kang et al. [10]	4.3	24.2	$2.54\lambda_0 \times 2.54\lambda_0 \times 0.3\lambda_0$
Vinnakota et al. [11]	17.8	17.2	$6\lambda_0 \times 6\lambda_0$
Baghel et al. [13]	17	14.6	$1.3\lambda_0 \times 0.94\lambda_0 \times 2\lambda_0$
Liu et al. [14]	1.7	11.8	$1.8\lambda_0 \times 1.8\lambda_0 \times 0.025\lambda_0$
Malik et al. [30]	9	13.8	$3.2\lambda_0 \times 2.3\lambda_0 \times 0.04\lambda_0$
Bito et al. [31]	3.3	5	$0.97\lambda_0 \times 0.97\lambda_0$
This work	6	11.3	$2.3\lambda_0 \times 1.45\lambda_0 \times 0.06\lambda_0$

[30] have a wider bandwidth. However, the transverse sizes in [11] and [30] are more than $3\lambda_0$ (λ_0 is the center wavelength). The profile in [13] is higher than $2\lambda_0$. Our work had a size of only $2.3\lambda_0 \times 1.45\lambda_0 \times 0.06\lambda_0$. Hence, despite a little sacrifice in bandwidth, the antenna used in this research needed less occupation space when compared with studies [11], [13], and [30]. A 6% bandwidth is enough to implement a WPT in the 5.8 ISM band. Several studies [5, 10, 14, 31] have narrower bandwidths than in our work. Furthermore, only a 5 dBi gain was obtained in [31]. A study of Chang et al. [5] has a maximum gain of only 2.71 dBi, and its bandwidth is only 4.6%.

Based on a fair comparison, our antenna had a good comprehensive performance (improved bandwidth, moderate gain, and smaller sizes) in the WPT system.

V. Conclusion

A planar substrate-integrated I-shaped slot grid antenna array was designed, fabricated, and measured. Two pieces of substrates were integrated to realize a compact structure. Four I-shaped slots were formed on the top PEC sheet to obtain a boresight high gain. A transverse stub and four narrow gaps were introduced to improve and refine the bandwidth. The working mechanism at 5.8 GHz was analyzed with the help of CM theory. Through measurements, the proposed antenna array exhibited good electrical properties in the 5.8 GHz ISM band. The measured bandwidth for $|S_{11}| < -10$ dB was 5% (5.67–5.96 GHz). The gain on boresight varied from 9.3 dBi to 11.3 dBi in the operating band. The cross-polarization level was less than −30 dB. Therefore, the proposed design is suitable for use as a transmitting antenna in a WPT system and in other scenarios with the requirements of planar, high integration, and high gain.

References

[1] H. Shoki, "Issues and initiatives for practical use of wireless power transmission technologies in Japan," in *Proceedings of 2011 IEEE MTT-S International Microwave Workshop Series on Innovative Wireless Power Transmission: Technologies, Systems, and Applications*, Kyoto, Japan, 2011, pp. 87-90. https://doi.org/10.1109/IMWS.2011.5877097

[2] S. Sasaki and K. Tanaka, "Wireless power transmission technologies for solar power satellite," in *Proceedings of 2011 IEEE MTT-S International Microwave Workshop Series on Innovative Wireless Power Transmission: Technologies, Systems, and Applications*, Kyoto, Japan, 2011, pp. 3-6. https://doi.org/10.1109/IMWS.2011.5877137

[3] X. Hou, Z. Wang, Y, Su, Z. Liu, and Z. Deng, "A dual-frequency dual-load multirelay magnetic coupling wireless power transfer system using shared power channel," *IEEE Transactions on Power Electronics*, vol. 37, no. 12, pp. 15717-15727, 2022. https://doi.org/10.1109/TPEL.2022.3190143

[4] R. Christen, U. Fischli, T. Franz, M. Schueller, and J. Smajic, "Wireless power transfer system for linear drives," in *Proceedings of 2022 23rd International Conference on the Computation of Electromagnetic Fields (COMPUMAG)*, Cancun, Mexico, 2022, pp. 1-4. https://doi.org/10.1109/COMPUMAG55718.2022.9827503

[5] X. L. Chang, P. S. Chee, and E. H. Lim, "Wearable flexible antenna for microwave wireless power transfer," in *Proceedings of 2022 IEEE 5th International Conference on Electronics Technology (ICET)*, Chengdu, China, 2022, pp. 757-761. https://doi.org/10.1109/ICET55676.2022.9825230

[6] D. Tang and Z. Chen, "Optimal frequency for implantable mid-field wireless power transfer," in *Proceedings of 2022 IEEE 5th International Conference on Electronics Technology (ICET)*, Chengdu, China, 2022, pp. 366-370. https://doi.org/10.1109/ICET55676.2022.9825368

[7] X. Han, W. Dong, and L. Cao, "The design of asymmetric wireless power transmission coils with limited-size," in *Proceedings of 2022 2nd Asia-Pacific Conference on Communications Technology and Computer Science (ACCTCS)*, Shenyang, China, 2022, pp. 279-284. https://doi.org/10.1109/ACCTCS53867.2022.00064

[8] L. Shi, N. Rasool, H. Zhu, K. Huang, and Y. Yang, "Design and experiment of a reconfigurable magnetic resonance coupling wireless power transmission system," *IEEE Microwave and Wireless Components Letters*, vol. 30, no. 7, pp. 705-708, 2020. https://doi.org/10.1109/LMWC.2020.2997068

[9] G. Oliveri, P. Rocca, F. Viani, F. Robol, and A. Massa, "Latest advances and innovative solutions in antenna array synthesis for microwave wireless power transmission," in *Proceedings of 2012 IEEE MTT-S International Microwave Workshop Series on Innovative Wireless Power Transmission: Technologies, Systems, and Applications*, Kyoto, Japan, 2012, pp. 71-73. https://doi.org/10.1109/IMWS.2012.6215822

[10] E. Kang, C. H. Seo, and H. Choo, "High gain array antenna using the high-order mode for wireless power transfer applications," in *Proceedings of 2020 IEEE Wireless Power Transfer Conference (WPTC)*, Seoul, South Korea, 2020, pp. 205-207. https://doi.org/10.1109/WPTC48563.2020.9295568

[11] S. S. Vinnakota, R. Kumari, H. Meena, and B. Majumder, "Rectifier integrated multibeam Luneburg lens employing artificial dielectric as a wireless power transfer medium at mm wave band," *IEEE Photonics Journal*, vol. 13, no. 3, article no. 5500314, 2021. https://doi.org/10.1109/JPHOT.2021.3079180

[12] J. H. Park, D. I. Kim, and K. W. Choi, "Analysis and experiment on multi-antenna-to-multi-antenna RF wireless power transfer," *IEEE Access*, vol. 9, pp. 2018-2031, 2020. https://doi.org/10.1109/ACCESS.2020.3047485

[13] A. K. Baghel, S. S. Kulkarni, and S. K. Nayak, "Far-field wireless power transfer using GRIN lens metamaterial at GHz frequency," *IEEE Microwave and Wireless Components Letters*, vol. 29, no. 6, pp. 424-426, 2019. https://doi.org/10.1109/LMWC.2019.2912056

[14] S. B. Liu, F. S. Zhang, M. Boyuan, S. P. Gao, and Y. X. Guo, "Multiband dual-polarized hybrid antenna with complementary beam for simultaneous RF energy harvesting and WPT," *IEEE Transactions on Antennas and Propagation*, vol. 70, no. 9, pp. 8485-8495, 2022. https://doi.org/10.1109/TAP.2022.3177484

[15] H. Wang, S. F. Liu, L. Chen, W. T. Li, and X. W. Shi, "Gain enhancement for broadband vertical planar printed antenna with H-shaped resonator structures," *IEEE Transactions on Antennas and Propagation*, vol. 62, no. 8, pp. 4411-4415, 2014. https://doi.org/10.1109/TAP.2014.2325955

[16] L. Leszkowska, M. Rzymowski, K. Nyka, and L. Kulas, "High-gain compact circularly polarized X-band superstrate antenna for CubeSat applications," *IEEE Antennas and Wireless Propagation Letters*, vol. 20, no. 11, pp. 2090-2094, 2021. https://doi.org/10.1109/LAWP.2021.3076673

[17] D. Guha, C. Sarkar, S. Dey, and C. Kumar, "Wideband high gain antenna realized from simple unloaded single patch," *IEEE Transactions on Antennas and Propagation*, vol. 63, no. 10, pp. 4562-4566, 2015. https://doi.org/10.1109/TAP.2015.2456942

[18] E. Baldazzi, A. Al-Rawi, R. Cicchetti, A. B. Smolders, O. Testa, C. D. J. van Coevorden Moreno and D. Caratelli, "A high-gain dielectric resonator antenna with plastic-based conical horn for millimeter-wave applications," *IEEE Antennas and Wireless Propagation Letters*, vol. 19, no. 6, pp. 949-953, 2020. https://doi.org/10.1109/LAWP.2020.2984565

[19] J. L. Liu, T. Su, and Z. X. Liu, "High-gain grating antenna with surface wave launcher array," *IEEE Antennas and Wireless Propagation Letters*, vol. 17, no. 4, pp. 706-709, 2018. https://doi.org/10.1109/LAWP.2018.2812918

[20] Z. Wang, G. X. Zhang, Y. Yin, and J. Wu, "Design of a dual-band high-gain antenna array for WLAN and WiMAX base station," *IEEE Antennas and Wireless Propagation Letters*, vol. 13, pp. 1721-1724, 2014. https://doi.org/10.1109/LAWP.2014.2352618

[21] M. Z. Ali and Q. U. Khan, "High gain backward scanning substrate integrated waveguide leaky wave antenna," *IEEE Transactions on Antennas and Propagation*, vol. 69, no. 1, pp. 562-565, 2021. https://doi.org/10.1109/TAP.2020.3006389

[22] J. Kraus, "A backward angle-fire array antenna," *IEEE Transactions on Antennas and Propagation*, vol. 12, no. 1, pp. 48-50, 1964. https://doi.org/10.1109/TAP.1964.1138171

[23] B. Zhang and Y. P. Zhang, "Grid array antennas with subarrays and multiple feeds for 60-GHz radios," *IEEE Transactions on Antennas and Propagation*, vol. 60, no. 5, pp. 2270-2275, 2012. https://doi.org/10.1109/TAP.2012.2189733

[24] Z. Chen, Y. P. Zhang, A. Bisognin, D. Titz, F. Ferrero, and C. Luxey, "An LTCC microstrip grid array antenna for 94-GHz applications," *IEEE Antennas and Wireless Propagation Letters*, vol. 14, pp. 1279-1281, 2015. https://doi.org/10.1109/LAWP.2015.2402159

[25] R. Garbacz and R. Turpin, "A generalized expansion for radiated and scattered fields," *IEEE Transactions on Antennas and Propagation*, vol. 19, no. 3, pp. 348-358, 1971. https://doi.org/10.1109/TAP.1971.1139935

[26] R. Harrington, J. Mautz, and Y. Chang, "Characteristic modes for dielectric and magnetic bodies," *IEEE Transactions on Antennas and Propagation*, vol. 20, no. 2, pp. 194-198, 1972. https://doi.org/10.1109/TAP.1972.1140154

[27] T. Bernabeu-Jimenez, A. Valero-Nogueira, F. Vico-Bondia, and A. A. Kishk, "A comparison between natural resonances and characteristic mode resonances of an infinite circular cylinder," *IEEE Transactions on Antennas and Propagation*, vol. 65, no. 5, pp. 2759-2763, 2017. https://doi.org/10.1109/TAP.2017.2670368

[28] M. Vogel, G. Gampala, D. Ludick, U. Jakobus, and C. J.

Reddy, "Characteristic mode analysis: putting physics back into simulation," *IEEE Antennas and Propagation Magazine*, vol. 57, no. 2, pp. 307-317, 2015. https://doi.org/10.1109/MAP.2015.2414670

[29] F. H. Lin and Z. N. Chen, "Low-profile wideband metasurface antennas using characteristic mode analysis," *IEEE Transactions on Antennas and Propagation*, vol. 65, no. 4, pp. 1706-1713, 2017. https://doi.org/10.1109/TAP.2017.2671036

[30] B. T. Malik, V. Doychinov, A. M. Hayajneh, S. A. R. Zaidi, I. D. Robertson, and N. Somjit, "Wireless power transfer system for battery-less sensor nodes," *IEEE Access*, vol. 8, pp. 95878-95887, 2020. https://doi.org/10.1109/ACCESS.2020.2995783

[31] J. Bito, V. Palazzi, J. Hester, R. Bahr, F. Alimenti, P. Mezzanotte, L. Roselli, and M. M. Tentzeris, "Millimeter-wave ink-jet printed RF energy harvester for next generation flexible electronics," in *Proceedings of 2017 IEEE Wireless Power Transfer Conference (WPTC)*, Taipei, Taiwan, 2017, pp. 1-4. https://doi.org/10.1109/WPT.2017.7953871

Zhiyi Li

received his M.E. degree in electromagnetic field and microwave technology from Xidian University, Xi'an, China, in 2016. Now, he is studying for a Ph.D. in radio physics at Sichuan University, Chengdu, China. From 2016–2018, he worked as an integration and verification engineer at Ericsson in Chengdu, China. His current research interests include electromagnetic metamaterials, antenna designs, numerical simulations, and wireless power transfer.

Shengjie Wang

was born in Anhui, China in 1989. He received a Ph.D. in optical engineering from the University of Electronic Science and Technology of China in 2020. He is currently a research associate with the CAAC Key Laboratory of Flight Techniques and Flight Safety, Civil Aviation Flight University of China. He mainly engages in laser communication and laser radar research. He is a member of the Chinese Optical Society and a member of the Chinese Society of Aeronautics and Astronautics.

Fan Li

received his Ph.D. in mathematical statistics from Sichuan University, China, in 2012. He was a post-doctoral researcher at the Laboratory of Prognostics and Health Management until July 2019. He is currently a research associate with the CAAC Key Laboratory of Flight Techniques and Flight Safety, Civil Aviation Flight University of China. His research interests are mainly based on the applications of big data analytics and artificial intelligence for intelligent civil aviation, including deep learning-based anomaly detection and precursor detection.

Lin Lin

received her M.S. degree from the University of Electronic Science and Technology of China in 2009. She is currently a senior engineer in the CAAC Key Laboratory of Flight Techniques and Flight Safety at the Civil Aviation Flight University of China. She is engaged in the research and development of ADS-B technology in the field of next-generation aviation navigation technology, and her main research directions include ADS-B, MLAT, Beidou, GPS, and the airworthiness of airborne equipment.

Hongzheng Zeng

received an M.S. degree in electronic science and technology from Chongqing University of Posts and Telecommunications of China, in 2014 and a Ph.D. in radio physics from Sichuan University of China, in 2020. He is currently a research associate in the CAAC Key Laboratory of Flight Technology and Flight Safety at the Civil Aviation Flight University of China. His research interests include numerical methods applied in electromagnetics, electromagnetic compatibility, and interference. He is an assistant electronic design engineer at the Chinese Institute of Electronics.